

A neural-network based nonlinear non-intrusive reduced basis method with online adaptation for parametrized partial differential equations

Jingye Li¹, Alex Bespalov¹, and Jinglai Li¹

¹School of Mathematics, University of Birmingham,
Birmingham, United Kingdom

Abstract

We propose a nonlinear, non-intrusive reduced basis method with online adaptation for efficient approximation of parametrized partial differential equations. The method combines neural networks with reduced-order modeling and physics-informed training to enhance both accuracy and efficiency. In the offline stage, reduced basis functions are obtained via nonlinear dimension reduction, and a neural surrogate is trained to map parameters to approximate solutions. The surrogate employs a nonlinear reconstruction of the solution from the basis functions, enabling more accurate representation of complex solution structures than linear mappings. The model is further refined during the online stage using lightweight physics-informed neural network training. This offline–online framework enables accurate prediction especially in complex scenarios or with limited snapshot data. We demonstrate the performance and effectiveness of the proposed method through numerical experiments.

Keywords: neural network, online adaptation, physics-informed neural network, reduced basis method

1 Introduction

Parametrized partial differential equations (PDEs) arise in a wide range of scientific and engineering applications, including uncertainty quantification, optimization, and control, where one must repeatedly solve the same PDE for many different parameter values [17, 28]. High-fidelity discretizations such as finite element, spectral, or finite difference methods can be prohibitively expensive in this many-query context. The reduced basis (RB) methods [17, 28] address this challenge by constructing, in an expensive offline stage, a low-dimensional approximation space tailored to the solution manifold, and then performing online solves in this reduced space. Since the online solves are performed in a reduced space, they are often significantly more efficient than solving the full PDE directly. While the standard RB methods can yield significant speedups, they still require the solution of algebraic systems at the online stage. This step can remain computationally demanding, particularly when the underlying PDE is nonlinear.

Non-intrusive RB approaches reduce computational cost during the online stage by replacing the traditional solver with a regression model that is constructed in the offline stage and directly maps parameters to RB coefficients. While noting that early works employ conventional interpolation methods (see, e.g., [5, 33]), our focus here is on more recent developments where trained neural networks (NN) are utilized to predict RB coefficients from parameters (see, e.g., [18, 32, 10]). While efficient, these non-intrusive methods rely on a surrogate model constructed entirely during the offline stage. Consequently, if the surrogate lacks sufficient accuracy or generalizes poorly, it may result in unreliable solution predictions, with no correction mechanism available during the online stage. To address this limitation, we propose a two-stage machine learning-based RB framework, which builds upon the non-intrusive RB approach while employing an online adaptation to enhance the solution for a given parameter value. In this novel approach, a non-intrusive surrogate model is trained in the offline stage and then refined in an unsupervised manner during the online phase to improve prediction accuracy. Importantly, the online refinement process is designed to remain computationally efficient, maintaining the low-cost advantage of non-intrusive RB methods.

Another important feature of the proposed method is its use of non-linear surrogate model. Standard RB methods and most of non-intrusive RB methods represent the solution as a linear combination of basis func-

tions, with some exceptions such as the autoencoder-based method proposed in [12]. While linear representations are computationally convenient, they can struggle to represent strongly nonlinear solution manifolds. In contrast, the proposed method constructs an NN-based nonlinear mapping of the basis functions, which can more effectively capture complex, nonlinear solution manifolds. This mapping is learned during the offline stage and subsequently adapted in the online stage. It is also worth mentioning that our method includes two main components in the offline stage. First, the reduced basis functions are obtained via an NN-based nonlinear dimension reduction. Second, model parameters enter the formulation through a hypernetwork of the main network that maps the reduced basis functions to the approximate solution.

As discussed earlier, online training plays a central role in the proposed method. Notably, this online training is performed within the framework of physics-informed neural networks (PINNs) [29, 3], which approximates PDE solutions by embedding residual minimization into the loss function of a neural network surrogate. A major advantage of our method is that, thanks to the offline computation, we can accurately approximate the solution with a lightweight network that can be trained efficiently. Specifically, only a small subset of the network parameters is adapted during the online stage, and the hypernetwork provides a well-informed ‘warm start’ that enables rapid convergence. More details are provided in Section 3.

To summarize, we propose an NN-based nonlinear RB method that combines the strengths of non-intrusive RB methods and online adaptation: in the offline stage, we obtain basis functions via a nonlinear dimension reduction and then train a neural network—whose weights are initialized by a parameter-dependent hypernetwork—to nonlinearly map these basis functions to the solution; in the online stage, we refine the prediction via a lightweight online PINN-like training. This hybrid framework provides enhanced accuracy with an efficient online training procedure.

The remainder of this work is organized as follows. Section 2 presents background material, including the parametrized PDE model of interest, standard and non-intrusive RB methods, and PINNs. Section 3 introduces the proposed NN-based nonlinear RB method, outlining its offline and online components in detail. Section 4 presents numerical experiments that demonstrate the effectiveness of the proposed method. Finally, Section 5 concludes the paper with a summary and potential directions for future research.

2 Background

2.1 Problem Setup

We consider a generic parametrized steady-state PDE system:

$$\mathcal{N}(u(\mathbf{x}; \boldsymbol{\mu}); \boldsymbol{\mu}) = 0, \quad \mathbf{x} \in \Omega, \quad (2.1a)$$

subject to a boundary condition (BC):

$$\mathcal{B}(u(\mathbf{x}; \boldsymbol{\mu}); \boldsymbol{\mu}) = 0, \quad \mathbf{x} \in \partial\Omega. \quad (2.1b)$$

Here, \mathcal{N} and \mathcal{B} are two differential operators, $u(\mathbf{x}; \boldsymbol{\mu})$ is the solution, \mathbf{x} is the d -dimensional spatial variable, and $\Omega \subset \mathbb{R}^d$ is the spatial domain with $\partial\Omega$ being its boundary; $\boldsymbol{\mu} \in \mathcal{Y}$ represents the collection of model parameters, with \mathcal{Y} being the parameter domain. For the sake of convenience, throughout this paper, we assume that the system consists of one primary PDE and one BC equation; however, the methods and techniques discussed here are applicable to systems with multiple PDEs and BC equations.

In many practical settings, $\boldsymbol{\mu}$ is modelled as a random variable with a prescribed probability distribution $\pi_{\boldsymbol{\mu}}(\cdot)$. Our objective is to numerically solve the parametrized PDE for a given value of $\boldsymbol{\mu}$. Conventionally, such PDEs are solved using standard numerical schemes such as the finite difference method (FDM), the finite element method (FEM), or spectral methods. Here, we present the Galerkin projection based FEM as an example (see, e.g., [19]). Let \mathcal{V} be a Hilbert space equipped with the inner product $(\cdot, \cdot)_{\mathcal{V}}$ and norm $\|\cdot\|_{\mathcal{V}}$. Its dual space is denoted by \mathcal{V}' , and the duality pairing is given by $\langle \cdot, \cdot \rangle_{\mathcal{V}', \mathcal{V}} : \mathcal{V}' \times \mathcal{V} \rightarrow \mathbb{R}$. We can view the differential operator \mathcal{N} in (2.1) as a mapping:

$$\mathcal{N} : \mathcal{V} \times \mathcal{Y} \longrightarrow \mathcal{V}'. \quad (2.2)$$

For a fixed parameter $\bar{\boldsymbol{\mu}} \in \mathcal{Y}$, the weak formulation of (2.1) is: find $u(\cdot; \bar{\boldsymbol{\mu}}) \in \mathcal{V}$ such that

$$\langle \tilde{\mathcal{N}}(u(\cdot; \bar{\boldsymbol{\mu}}); \bar{\boldsymbol{\mu}}), v \rangle_{\mathcal{V}', \mathcal{V}} = 0 \quad \forall v \in \mathcal{V}, \quad (2.3)$$

with $\tilde{\mathcal{N}}$ representing both the operator \mathcal{N} in Eq. (2.1) and the BC operator \mathcal{B} in Eq. (2.1b).

Next the solution $u \in \mathcal{V}$ is approximated in a finite-dimensional subspace $\mathcal{V}_n \subset \mathcal{V}$, spanned by n basis functions $\{\eta_1, \eta_2, \dots, \eta_n\}$. The approximate

solution is expressed as a linear combination:

$$u_h(\mathbf{x}; \bar{\boldsymbol{\mu}}) = \sum_{j=1}^n \tilde{u}_j(\bar{\boldsymbol{\mu}}) \eta_j(\mathbf{x}), \quad (2.4)$$

and we seek the coefficient vector

$$\tilde{\mathbf{u}}(\bar{\boldsymbol{\mu}}) = [\tilde{u}_1(\bar{\boldsymbol{\mu}}) \quad \dots \quad \tilde{u}_n(\bar{\boldsymbol{\mu}})]^T \in \mathbb{R}^n, \quad (2.5)$$

such that

$$\langle \tilde{\mathcal{N}}(u_h(\cdot; \bar{\boldsymbol{\mu}}); \bar{\boldsymbol{\mu}}), v_h \rangle_{\mathcal{V}', \mathcal{V}} = 0 \quad \forall v_h \in \mathcal{V}_n. \quad (2.6)$$

Since \mathcal{V}_n is spanned by basis functions $\{\eta_1, \eta_2, \dots, \eta_n\}$, Eq. (2.6) is equivalent to

$$\langle \tilde{\mathcal{N}}(u_h(\cdot; \bar{\boldsymbol{\mu}}); \bar{\boldsymbol{\mu}}), \eta_j \rangle_{\mathcal{V}', \mathcal{V}} = 0, \quad j = 1, \dots, n. \quad (2.7)$$

Next we need to solve the equation system (2.7). If $\tilde{\mathcal{N}}$ is a linear operator, it reduces to an $n \times n$ linear system. If $\tilde{\mathcal{N}}$ is nonlinear, a common approach is to solve the equation system using a linearization procedure (e.g., the Newton's method [11]).

The presumption here is that we use a sufficiently large number of basis functions so that the numerical approximate solution u_h is of high accuracy and is referred to as the *high-fidelity solution* in this paper. To achieve such accuracy, the number of basis functions required is often very large, which in turn leads to a very high-dimensional algebraic equation system in Eq. (2.7). Assembling and solving such a large system—especially using iterative linearization in the case of a nonlinear operator—becomes computationally expensive in terms of both memory and CPU time. To this end, the RB method is a popular approach for solving parametrized PDEs, as it can often significantly reduce the dimensionality of the algebraic equation system.

2.2 Reduced basis method

In this section, we give a brief overview of the RB method. The main idea of the method is rather straightforward: first, we construct a low-dimensional approximation space that is specifically tailored to capture the essential features of the solution manifold across the parameter space, and then we solve the PDE for a specific parameter value in this reduced low-dimensional space, significantly lowering computational costs compared to the standard

approaches. The standard RB method is implemented in two stages: an *offline stage* and an *online stage*. In the offline stage, the reduced-dimensional space for solution approximation is constructed. This stage is computationally expensive but performed only once. In the online stage, the reduced space obtained offline is used to rapidly approximate solutions for new parameter values, enabling real-time simulations of the PDE model.

2.2.1 Offline stage

The first step in the offline stage is to compute a set of high-fidelity solutions, often called snapshots, corresponding to some selected parameter values. In practice, one usually randomly generates the parameter values from the underlying distribution of the parameter:

$$\{\boldsymbol{\mu}^{(1)}, \boldsymbol{\mu}^{(2)}, \dots, \boldsymbol{\mu}^{(n_s)}\}, \text{ with } \boldsymbol{\mu}^{(i)} \sim \pi_{\boldsymbol{\mu}}(\cdot) \text{ for } i = 1, \dots, n_s.$$

For each parameter value $\boldsymbol{\mu}^{(i)}$, we compute the high-fidelity solution using a standard numerical method (e.g., the Galerkin method discussed in Section 2.1). Let the high-fidelity solutions for each parameter value be denoted as

$$u_h(\cdot; \boldsymbol{\mu}^{(i)}), \quad i = 1, 2, \dots, n_s; \quad (2.8)$$

these are represented as in Eq. (2.4), and the coefficient vectors $\tilde{\mathbf{u}}_h(\boldsymbol{\mu}^{(i)})$ are given by Eq. (2.5). We restate that $\tilde{\mathbf{u}}_h(\boldsymbol{\mu}^{(i)})$ are n -dimensional vectors, and they form the snapshot matrix \mathbf{S} :

$$\mathbf{S} = [\tilde{\mathbf{u}}_h(\boldsymbol{\mu}^{(1)}) \quad \tilde{\mathbf{u}}_h(\boldsymbol{\mu}^{(2)}) \quad \dots \quad \tilde{\mathbf{u}}_h(\boldsymbol{\mu}^{(n_s)})] \in \mathbb{R}^{n \times n_s}. \quad (2.9)$$

Next, we build the reduced space using these snapshots, often via the proper orthogonal decomposition (POD) technique [17, 28]. Specifically, we perform the singular value decomposition (SVD) of the snapshot matrix \mathbf{S} :

$$\mathbf{S} = \mathbf{B}\boldsymbol{\Sigma}\mathbf{V}^T, \quad (2.10)$$

where $\mathbf{B} \in \mathbb{R}^{n \times n}$, $\boldsymbol{\Sigma} \in \mathbb{R}^{n \times n_s}$ (diagonal matrix containing singular values), and $\mathbf{V} \in \mathbb{R}^{n_s \times n_s}$. We select the first $r \ll n$ singular vectors corresponding to the largest singular values to construct the reduced basis functions:

$$\psi_i(\mathbf{x}) = \sum_{j=1}^n \mathbf{B}_{j,i} \eta_j(\mathbf{x}), \quad i = 1, \dots, r, \quad (2.11)$$

where $\{\eta_j(\mathbf{x})\}_{j=1}^n$ are the original basis functions from the high-fidelity solution space. The reduced basis space is thus defined by

$$\mathcal{V}_r = \text{span}\{\psi_1, \psi_2, \dots, \psi_r\}, \quad (2.12)$$

and in the online stage, that is described next, we will compute the *reduced solution* as an element of \mathcal{V}_r .

2.2.2 Online stage

Once the reduced space $\mathcal{V}_r = \text{span}\{\psi_1, \dots, \psi_r\}$ has been constructed in the offline stage, the online stage aims to compute an efficient approximation of the high-fidelity solution for a new parameter value $\boldsymbol{\mu}^* \in \mathcal{Y}$. We seek a reduced solution $u_{\text{rb}}(\mathbf{x}, \boldsymbol{\mu}^*) \in \mathcal{V}_r$ expressed as a linear combination of the reduced basis functions:

$$u_{\text{rb}}(\mathbf{x}, \boldsymbol{\mu}^*) = \tilde{u}_1(\boldsymbol{\mu}^*)\psi_1(\mathbf{x}) + \dots + \tilde{u}_r(\boldsymbol{\mu}^*)\psi_r(\mathbf{x}), \quad (2.13)$$

and our goal now is to compute the coefficient vector:

$$\tilde{\mathbf{u}}_{\text{rb}}(\boldsymbol{\mu}^*) = [\tilde{u}_1(\boldsymbol{\mu}^*) \quad \dots \quad \tilde{u}_r(\boldsymbol{\mu}^*)]^T \in \mathbb{R}^r. \quad (2.14)$$

Here we can use, for example, the Galerkin projection method, except that we now construct the solution in the reduced space \mathcal{V}_r , rather than in \mathcal{V}_n . Namely, Eq. (2.7) becomes

$$\langle \tilde{\mathcal{N}}(u_{\text{rb}}(\cdot, \boldsymbol{\mu}^*); \boldsymbol{\mu}^*), \psi_j \rangle_{\mathcal{V}', \mathcal{V}} = 0, \quad j = 1, \dots, r, \quad (2.15)$$

where u_{rb} is given by Eq. (2.13). Therefore, using the reduced bases, we obtain a system of r algebraic equations, compared to a system of n equations in the original Galerkin projection method. In many practical problems, r is much smaller than n , which can result in significant computational savings. When the underlying algebraic equations are linear and certain conditions are satisfied, the resulting linear system can be solved very efficiently, despite the fact that the associated system matrix is, in general, dense. Even in nonlinear cases, the method still improves efficiency due to the substantially reduced system size (see, e.g., [4, 6]).

2.2.3 Non-intrusive RB methods

In the standard RB method, especially when the system is nonlinear, equations (2.15) need to be solved numerically at the online stage. This reduced

system is much less expensive than the original system, but may still require rather substantial computational time.

To this end, the non-intrusive RB methods are proposed to further reduce the online computational cost. The basic idea behind these methods is rather straightforward: instead of solving for the coefficient at the online stage, one imposes a regression model representing the coefficients $\tilde{\mathbf{u}}_{\text{rb}}$ as a function of the model parameter $\boldsymbol{\mu}$, which is trained at the offline stage with additional high-fidelity solution data. We refer to [34, 26] for more comprehensive reviews of the non-intrusive RB methods. The non-intrusive RB methods do not require solving the reduced problem in online stage, and thus make the online computation much faster. As mentioned earlier, we here focus on methods that use NN models to compute the reduced solutions, while noting that other surrogate models are also available [5, 15, 16]. In [18, 7], high-fidelity solutions for a set of parameter values are used as labeled data to train an NN with parameter as input and coefficient vector as output. The basic procedure of the method is the following:

1. Generate the reduced basis $\{\psi_1, \dots, \psi_r\}$ using the same procedure as in the standard RB method.
2. Write the RB solution as Eq. (2.13) with the coefficient $\tilde{\mathbf{u}}_{\text{rb}}$ given by Eq. (2.14).
3. Assume an NN model $\tilde{\mathbf{u}}_{\text{rb}}(\boldsymbol{\mu}) = G(\boldsymbol{\mu}; \boldsymbol{\theta}_G)$, where $\boldsymbol{\theta}_G$ are the model parameters.
4. Sample a new set of n_G parameter values $\boldsymbol{\mu}^{(1)}, \dots, \boldsymbol{\mu}^{(n_G)}$ and compute the associated high-fidelity solutions $u_h(\mathbf{x}, \boldsymbol{\mu}^{(1)}), \dots, u_h(\mathbf{x}, \boldsymbol{\mu}^{(n_G)})$.
5. Construct the labeled training data: $(\boldsymbol{\mu}^{(1)}, \tilde{\mathbf{u}}^{(1)}), \dots, (\boldsymbol{\mu}^{(n_G)}, \tilde{\mathbf{u}}^{(n_G)})$, where $\tilde{\mathbf{u}}^{(i)}$ denotes the coefficients of $u_h(\mathbf{x}, \boldsymbol{\mu}^{(i)})$ projected onto the reduced basis functions ψ_1, \dots, ψ_r .
6. Estimate $\boldsymbol{\theta}_G$ by minimizing the supervised loss function:

$$L_{\text{RB}}(\boldsymbol{\theta}_G) = \sum_{i=1}^{n_G} \|\tilde{\mathbf{u}}^{(i)} - G(\boldsymbol{\mu}^{(i)}; \boldsymbol{\theta}_G)\|^2.$$

Several variants of the method have been developed as well. For example, the number of labelled data required to train the network can be reduced

if the physics-informed loss is added to the training loss [8]. Other variants of NN based non-intrusive RB include [13], which constructs the NN model using autoencoder architectures, [27], where graph-based approaches have been proposed to handle unstructured spatial domains.

2.3 Physics-informed neural networks

In this section we review the physics-informed neural networks (PINNs), another important ingredient of our method. PINNs [29] are a class of machine learning based methods for the numerical solution of PDEs. Suppose we want solve the boundary value problem (2.1). When using PINN, the solution to (2.1) is approximated by an NN $u_{\text{NN}}(\mathbf{x}; \boldsymbol{\theta})$ with $\boldsymbol{\theta}$ being the network parameters. Since $u_{\text{NN}}(\mathbf{x}; \boldsymbol{\theta})$ is only an approximate solution of Eq. (2.1) and it does not satisfy the equation exactly, we can compute the residuals as

$$\begin{aligned} \mathcal{N}[u_{\text{NN}}(\mathbf{x}; \boldsymbol{\theta}); \boldsymbol{\mu}], \quad \mathbf{x} \in \Omega, \\ \mathcal{B}[u_{\text{NN}}(\mathbf{x}; \boldsymbol{\theta}); \boldsymbol{\mu}], \quad \mathbf{x} \in \partial\Omega. \end{aligned} \quad (2.16)$$

The basic idea here is that we should train the network $u_{\text{NN}}(\mathbf{x}; \boldsymbol{\theta})$ to minimize the residuals, which can be measured using a loss function based either on the strong or weak form. Here, we present the strong form based loss function, as it is used in our numerical implementation:

$$L_{\text{PINN}}(\boldsymbol{\theta}) = \|\mathcal{N}[u_{\text{NN}}(\mathbf{x}; \boldsymbol{\theta})]\|_{\Omega}^2 + \lambda \|\mathcal{B}[u_{\text{NN}}(\mathbf{x}; \boldsymbol{\theta})]\|_{\partial\Omega}^2, \quad (2.17)$$

where λ is a positive coefficient, and $\|\cdot\|_{\Omega}^2$ and $\|\cdot\|_{\partial\Omega}^2$ are the L^2 -norms defined on Ω and $\partial\Omega$ respectively. In practice, a discrete version of the loss function is often used:

$$\hat{L}_{\text{PINN}}(\boldsymbol{\theta}) = \sum_{i=1}^{m_1} (\mathcal{N}[u_{\text{NN}}(\mathbf{x}_i; \boldsymbol{\theta})])^2 + \lambda \sum_{i=1}^{m_2} (\mathcal{B}[u_{\text{NN}}(\mathbf{x}'_i; \boldsymbol{\theta})])^2, \quad (2.18)$$

where $\mathbf{x}_1, \dots, \mathbf{x}_{m_1}$ are samples drawn uniformly from the spatial domain Ω , and $\mathbf{x}'_1, \dots, \mathbf{x}'_{m_2}$ are drawn uniformly from the boundary $\partial\Omega$.

To approximate the solution, PINNs typically employ a Multi-Layer Perceptron (MLP) network, consisting of an input layer, multiple hidden layers, and a single output layer [14]. Each layer is made up of a number of neurons which are connected to those in adjacent layers. PINNs often employ deep architectures with a substantial number of neurons to effectively capture complex solution structure. For example, in their seminal work [29], the

authors utilized a neural network with 9 layers, each containing 20 neurons, to solve the Navier–Stokes equation, and one with 4 hidden layers of 200 neurons each for the Allen–Cahn equation.

3 Nonlinear RB method with online adaptation

3.1 Motivation

We discuss the motivation of our method from the PINNs perspective. PINNs are often computationally intensive when applied to complex PDE models: firstly, in order to accurately approximate solutions to such models, the neural network typically needs to be large in both depth and width, and secondly, a substantial number of training iterations is often required to achieve a satisfactory solution of the associated minimization problem. To this end, similar to standard RB methods, which use offline computation to accelerate conventional PDE solvers (such as FEM) in the online stage, the proposed method uses offline computation to accelerate PINNs at the online stage. Specifically, during the offline stage, our method constructs an effective reduced basis so that the solution can be approximated by a light-weight network, providing at the same time a ‘warm start’ for the training process.

3.2 Offline Stage: a non-intrusive RB formulation

The offline stage of our method is very similar to that in the non-intrusive RB methods. Recall that in the non-intrusive RB framework, the main task of the offline stage is two-fold: first, it constructs the reduced bases from the snapshots; second, it builds the regression model from the parameters to the RB coefficients, which can then be used to obtain the reduced solution directly. This task remains the same in the offline stage of our method, but there are two main differences. First, the dimension reduction process is nonlinear and data-driven. Second, unlike the standard and non-intrusive RB methods, which assume that the reduced solution is a linear combination of the basis functions, our approach employs a nonlinear mapping from the basis functions to the reduced solution.

The starting point of our method is the same as for the standard reduced basis methods: generate a set of snapshots and obtain the reduced basis $\{\psi_1, \dots, \psi_\ell\}$ via POD. Here, we refer to $\{\psi_1, \dots, \psi_\ell\}$ as the “initial reduced basis”, and the actual reduced basis, denoted by $\{\phi_1, \dots, \phi_r\}$, is obtained

through a nonlinear mapping of the initial ones:

$$[\phi_1, \dots, \phi_r] = \Phi(\psi_1, \dots, \psi_\ell), \quad (3.1)$$

where $r \leq \ell$ is the number of the actual reduced basis functions. In the implementation this nonlinear mapping Φ is represented by an NN model with parameter θ_Φ . Next, we assume that the reduced solution is a nonlinear mapping of the actual basis functions, constructed using a neural network U with parameter θ_U :

$$u_{\text{rb}}(\mathbf{x}) = U(\phi_1, \dots, \phi_r; \theta_U). \quad (3.2)$$

The neural network model U should be kept shallow and narrow to maintain simplicity and efficiency. Recall that the solution depends on the PDE parameter μ , and in our method, parameter μ enters the formulation through the network parameter θ_U . Namely we write θ_U as:

$$\theta_U = \Theta(\mu; \theta_\Theta), \quad (3.3)$$

where $\Theta(\cdot; \theta_\Theta)$ is a neural network with parameter θ_Θ . That is, Θ is used as a hypernetwork for U . We emphasize that model Φ does not depend on μ , implying that the reduced basis functions ϕ_1, \dots, ϕ_r are independent of μ . The entire model architecture is illustrated by Fig 1.

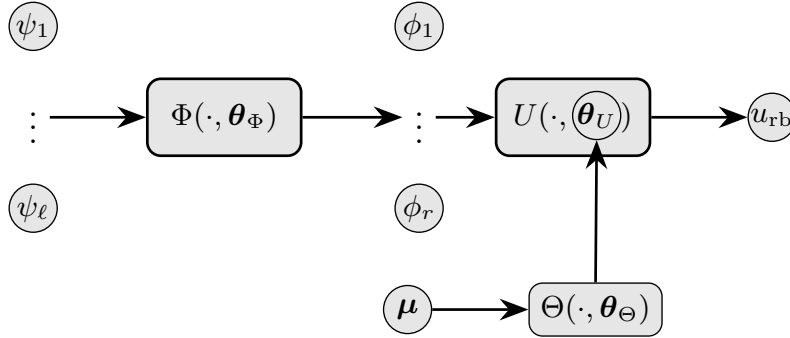


Figure 1: The offline training procedure and the network architecture.

To summarize, our model consists of three NNs: the *dimension reduction* model Φ , the *solution reconstruction* model U and the *parameter estimation*

model Θ . For conciseness we refer to the entire model as $F(\psi_1, \dots, \psi_\ell, \boldsymbol{\mu}; \boldsymbol{\theta})$ with network parameters $\boldsymbol{\theta}$ and, as a result, we have

$$u_{\text{rb}}(\mathbf{x}, \boldsymbol{\mu}; \boldsymbol{\theta}) = F(\psi_1, \dots, \psi_\ell, \boldsymbol{\mu}; \boldsymbol{\theta}). \quad (3.4)$$

Similar to the non-intrusive RB, the network is trained in a supervised manner. Namely we generate a new set of n_F labelled data:

$$(\boldsymbol{\mu}^{(1)}, u_h(\boldsymbol{\mu}^{(1)})), \dots, (\boldsymbol{\mu}^{(n_F)}, u_h(\boldsymbol{\mu}^{(n_F)})).$$

For training, we use a loss function which encodes information about the solution and its derivatives. We assume that the reduced solution u_{rb} lives in the Sobolev space $H^p(\Omega)$ and define the offline loss function using the weighted $H^p(\Omega)$ -norm:

$$L_{\text{offline}}(\boldsymbol{\theta}) = \sum_{i=1}^{n_F} \sum_{|\alpha| \leq p} \lambda_\alpha \int_{\Omega} |D^\alpha u_{\text{rb}}(\mathbf{x}, \boldsymbol{\mu}^{(i)}; \boldsymbol{\theta}) - D^\alpha u_h(\mathbf{x}, \boldsymbol{\mu}^{(i)})|^2 d\mathbf{x}, \quad (3.5)$$

where $\lambda_\alpha \geq 0$ are weights for each derivative term, $\alpha = (\alpha_1, \dots, \alpha_d) \in \mathbb{N}_0^d$ is a multi-index, $|\alpha| = \sum_{i=1}^d \alpha_i$, and D^α is the mixed partial derivative operator defined as,

$$D^\alpha = \frac{\partial^{|\alpha|}}{\partial x_1^{\alpha_1} \dots \partial x_d^{\alpha_d}}.$$

As such, at the offline stage, the model F is trained by minimizing the loss function (3.5).

3.3 Online stage: network adaptation

Through the offline stage, we have obtained a model F which can be used directly to predict the solution for a given parameter value $\boldsymbol{\mu}^*$. However, this model may not be sufficiently accurate, especially for parameter values in regions with sparse training data. To further improve the prediction accuracy, we propose to conduct unsupervised learning to adapt the model during the online stage, using a formulation similar to that of PINNs.

In the offline stage, we have trained three networks: the dimension reduction network Φ , the solution reconstruction network U , and the parameter estimation network Θ . In the online stage, the dimension reduction network is frozen, which means that the reduced basis functions obtained in the offline stage are used directly. We seek to adapt the solution reconstruction

model $U(\phi_1, \dots, \phi_r; \boldsymbol{\theta}_U)$ in an unsupervised manner. Recall that the reduced solution $u_{\text{rb}}(\mathbf{x})$ is in the form of Eq. (3.2), and we plug it into the discrete PINNs loss (2.18), yielding our online loss function

$$L_{\text{online}}(\boldsymbol{\theta}_U) = \sum_{i=1}^{m_1} (\mathcal{N}[U(\phi_1(\mathbf{x}_i), \dots, \phi_r(\mathbf{x}_i); \boldsymbol{\theta}_U)])^2 + \lambda \sum_{i=1}^{m_2} (\mathcal{B}[U(\phi_1(\mathbf{x}_i), \dots, \phi_r(\mathbf{x}_i); \boldsymbol{\theta}_U)])^2 + R(\boldsymbol{\theta}), \quad (3.6)$$

where the sampling points $\{\mathbf{x}_i\}_{i=1}^{m_1}$ and $\{\mathbf{x}_i\}_{i=1}^{m_2}$ are generated in the same manner as in standard PINNs, and $R(\boldsymbol{\theta})$ is a regularization term that will be defined later.

Now let $\boldsymbol{\theta}_U^*$ be the output of the parameter estimation model obtained at the offline stage:

$$\boldsymbol{\theta}_U^* = \Theta(\boldsymbol{\mu}^*; \boldsymbol{\theta}_\Theta),$$

and it will be used in the two capacities: for regularization and for initialization. First the regularizer $R(\boldsymbol{\theta})$ is defined as:

$$R(\boldsymbol{\theta}) = \gamma \|\boldsymbol{\theta}_U - \boldsymbol{\theta}_U^*\|_2^2,$$

where $\gamma \geq 0$ is the regularization coefficient. Here, we adopt a decaying regularization strategy by making γ iteration-dependent, i.e., $\gamma = \gamma_k$, where k denotes the epoch number. The regularization weight γ_k is designed to decrease over time, satisfying $\gamma_k \rightarrow 0$ as $k \rightarrow \infty$. Next, Eq. (3.6) is minimized by using $\boldsymbol{\theta}_U^*$ as the initial guess. The online training procedure and the network architecture are shown in Fig. 2.

It is important to note that online training typically can be carried out very efficiently, and the reason for this is two-fold. First, as mentioned in Section 3.2, the network U has been deliberately kept small in both depth and width, and so the dimensionality of the parameter space is modest. For example, in Section 4.1, a network with a single hidden layer of 5 neurons is used to reconstruct the solution of the Burgers' equation. Second, in most cases, $\boldsymbol{\theta}_U^*$ provides a good initial guess for the training procedure, so that the number of iterations can be significantly reduced.

4 Numerical experiments

We present two numerical examples in this section, with implementation details provided in the Appendix.

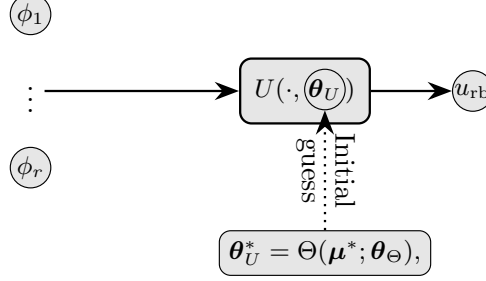


Figure 2: The online training procedure and the network architecture.

4.1 Burgers' equation

Our first example is the one-dimensional Burgers' equation over $\Omega = [-1, 1]$:

$$\begin{aligned} u(x, \boldsymbol{\mu}) \frac{\partial u(x, \boldsymbol{\mu})}{\partial x} - \frac{\partial^2 u(x, \boldsymbol{\mu})}{\partial x^2} &= s(x, \boldsymbol{\mu}), \\ u(-1, \boldsymbol{\mu}) &= u(1, \boldsymbol{\mu}) = 0, \end{aligned} \quad (4.1)$$

where $s(\mathbf{x}, \boldsymbol{\mu})$ is the source term and $\boldsymbol{\mu}$ is a two dimensional parameter $\boldsymbol{\mu} = [\mu_1, \mu_2]^T$ following a uniform distribution defined on $[1, 10] \times [1, 10]$. In this example we choose the source term to be

$$\begin{aligned} s(\mathbf{x}, \boldsymbol{\mu}) &= (1 + \mu_1 x)^2 \left[6x^2 - 2 - \frac{2h^2\mu_2^2}{9} (x^2 - 1)^2 \right] \cos\left(\frac{2h\mu_2 x}{3}\right) \\ &+ \frac{2h\mu_2}{3} (1 + \mu_1 x) (x^2 - 1) [\mu_1 (x^2 - 1) + 2x(1 + \mu_1 x)] \sin\left(\frac{2h\mu_2 x}{3}\right) \\ &- (6x^2 - 2) (1 + \mu_1 x)^2, \end{aligned}$$

and it follows that Eq. (4.1) admits the exact solution given by

$$u_{\text{ex}}(x, \boldsymbol{\mu}) = (1 + \mu_1 x) \sin\left(-\kappa \frac{\mu_2 x}{3}\right) (x^2 - 1). \quad (4.2)$$

Note that in Eq. (4.2) κ is a positive parameter controlling the “frequency” of the solution, i.e., how rapidly it varies with respect to x . To demonstrate the effect of κ , Fig. 3 shows two sample solutions corresponding to $\kappa = 1$ and $\kappa = 9$ (both with $\mu_1 = \mu_2 = 5$), respectively. As shown in the figure, the solution exhibits more rapid variation for larger κ , making it intuitively

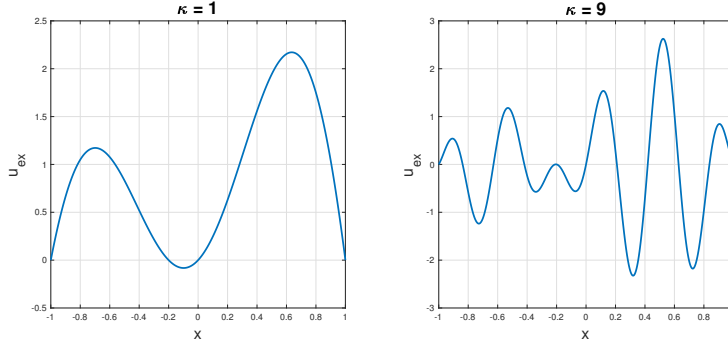


Figure 3: Exact solutions of Eq. (4.1) for $\kappa = 1$ (left) and $\kappa = 9$ (right).

more challenging to approximate. In this example, we will evaluate the performance of the proposed method for both $\kappa = 1$ and $\kappa = 9$.

In all numerical experiments, we ensure that the set of snapshots is sufficiently large so that it does not become a major limiting factor in performance: the sample size is 100 for $\kappa = 1$, and 1600 for $\kappa = 9$. We first examine the network model obtained solely from the offline computation. In Fig. 4, we plot the relative mean-squared errors of the reduced solutions versus the number of basis functions for both $\kappa = 1$ and $\kappa = 9$. The errors are computed using 100 randomly generated test samples. In addition to the results of the proposed method, we show two reference results for comparison. The first is the optimal linear projection, obtained by projecting the exact solution onto the reduced basis; it represents the best-case scenario when a linear mapping is used. The second is the result of the non-intrusive RB method, which, as discussed earlier, is also based on linear mappings. For the less oscillatory case ($\kappa = 1$), we observe that the error in the optimal linear projection decays rapidly, becoming smaller than that of our method when six or more basis functions are used. This suggests that in such a simple setting, a linear mapping is capable of approximating the solution quite well. Obviously the optimal projection serves as an ideal benchmark, rather than a practical method. When comparing the results of our nonlinear RB method with those of the linear-mapping-based non-intrusive RB, we can see that the former consistently yields smaller errors, demonstrating the advantage of incorporating nonlinearity in the reduced model. The advantage of the nonlinear mapping becomes more evident in the case of $\kappa = 9$. In this more challenging setting, our method not only significantly outperforms the non-

intrusive RB method, but also achieves considerably lower errors than the optimal linear projection when using up to 20 basis functions. This highlights the effectiveness of nonlinear representations in capturing complex solution behavior.

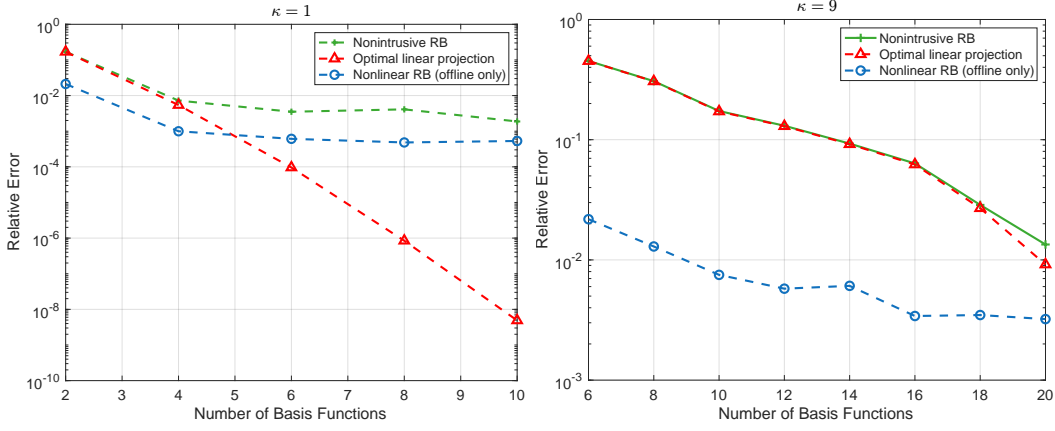


Figure 4: Relative errors of the offline-computed solutions as a function of the number of basis functions. Left for the case $\kappa = 1$, and right for the case $\kappa = 9$.

Next, we consider the effect of online network adaptation, which is a key distinction between our method and the non-intrusive RB method. The first question we aim to address is whether such online computation is necessary. To this end, we plot in Fig. 5 the histogram of the relative errors of the reduced solutions obtained by the offline training only. For $\kappa = 1$, we use $r = 8$ basis functions, and for $\kappa = 9$, we set $r = 16$. The results show that the offline model performs very well in the simpler case ($\kappa = 1$), but less effectively in the more challenging case ($\kappa = 9$). If we use 10^{-3} as a threshold for acceptable accuracy, nearly all test cases—94 out of 100—satisfy this criterion for $\kappa = 1$, while for $\kappa = 9$, only 3 out of 100 cases fall below it. From this we can conclude that online adaptation is particularly important for more complex solutions. Therefore, let us now focus on examining the effect of online adaptation in the $\kappa = 9$ case. In Fig. 6 we compare the errors of the reduced solutions obtained by the offline training only and those updated with online adaptation. The left panel shows the average errors for all 100 test samples, while the right panel focuses on the worst cases – that is, the 10% of samples with the largest offline errors. In both cases, online adaptation leads to im-

proved accuracy of the RB solution, with the improvement being particularly significant for the worst cases where the offline model alone performs poorly. These results demonstrate that online adaptation is highly useful, especially when the offline model fails to capture the solution accurately.

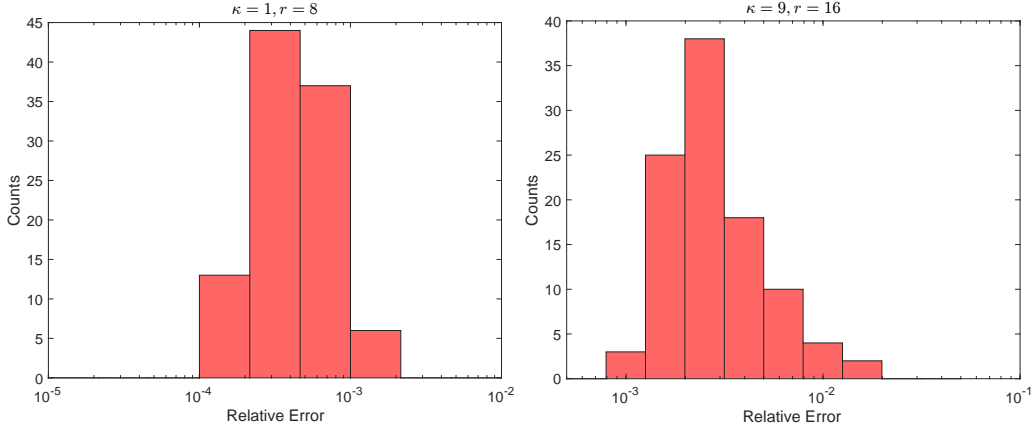


Figure 5: Histograms of the relative errors of the offline-computed solutions over 100 test samples. Left for the case $\kappa = 1$ using 8 basis functions; right for the case $\kappa = 9$ using 16 basis functions.

4.2 Lid-driven cavity problem

In this section, we consider a more challenging example—the lid-driven cavity problem, which is a widely used benchmark in computational fluid dynamics [1, 2]. We are looking to solve a parametrized version of this problem, which is a challenging task for the following reasons: (1) it involves a complex and computationally intensive parameter-dependent PDE system, (2) the computational domain and the boundary conditions are parameter dependent, and (3) the associated parameter domain is high-dimensional. Specifically, we are looking to compute the velocity and pressure fields of a viscous flow within a parallelogram-shaped domain (where the angle between the horizontal and slanted edges is a random parameter), subject to parametrized boundary conditions. This problem has been used as a test example in several RB-related works such as [18, 8].

The problem is governed by the following equations:

$$\begin{cases} \nabla \cdot \mathbf{u} = 0, & \mathbf{x} \in \Omega(\theta), \\ -\frac{1}{Re} \Delta \mathbf{u} + (\mathbf{u} \cdot \nabla) \mathbf{u} + \nabla p = \mathbf{0}, & \mathbf{x} \in \Omega(\theta), \end{cases} \quad (4.3)$$

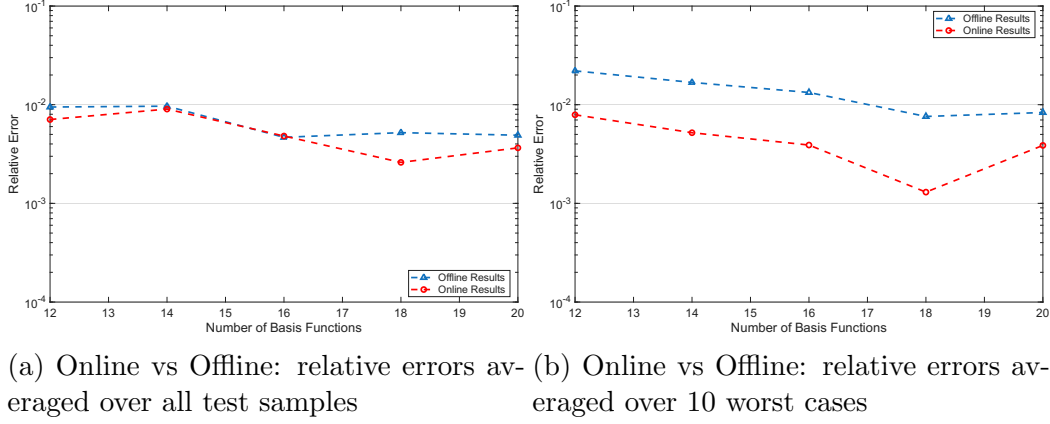


Figure 6: Relative errors of the solutions reconstructed using the offline stage only versus those with online adaptation.

where $\mathbf{u} = (u, v)^\top$ is the velocity field, p is the pressure, Re is the Reynolds number, and $\Omega(\theta)$ denotes the computational domain. The domain $\Omega(\theta)$ is a parallelogram centered at the origin, with the length of all edges being 1, and θ being the angle between the base and the slanted edge (see Fig. 7). The boundary of the domain, denoted by Γ , is composed of the lid (i.e., the top horizontal edge) Γ_2 and the walls (the three other edges of the parallelogram) Γ_1 . The boundary conditions are given by

$$u(\mathbf{x}) = \begin{cases} (2x_1 - \cos \theta + 1 + R(2x_1 - \cos \theta))^2 \\ \quad \times (2x_1 - \cos \theta - 1 - R(2x_1 - \cos \theta))^2, & \text{if } \mathbf{x} \in \Gamma_2(\theta), \\ 0, & \text{if } \mathbf{x} \in \Gamma_1(\theta), \end{cases}$$

and

$$v(\mathbf{x}) = 0, \quad \mathbf{x} \in \Gamma,$$

where

$$R(x) = 0.001 \sum_{i=1}^{10} \alpha_i \sin(i\pi x) \cos(i\pi x). \quad (4.4)$$

The parameters in this PDE model are the domain angle θ , the Reynolds number Re , and the boundary condition coefficients $\boldsymbol{\alpha} = (\alpha_1, \dots, \alpha_{10})$; thus, overall, the parameter domain is twelve-dimensional. All these parameters are the images of independent uniformly distributed random variables; specifically, $\theta \sim U[\frac{\pi}{3}, \frac{2\pi}{3}]$, $Re \sim U[100, 200]$, and $\boldsymbol{\alpha} \sim U[-1, 1]^{10}$.

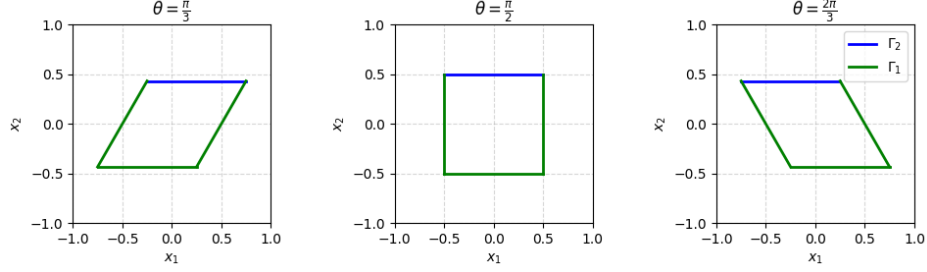


Figure 7: Examples of the computational domain $\Omega(\theta)$ with $\theta \in \{\pi/3, \pi/2, 2\pi/3\}$.

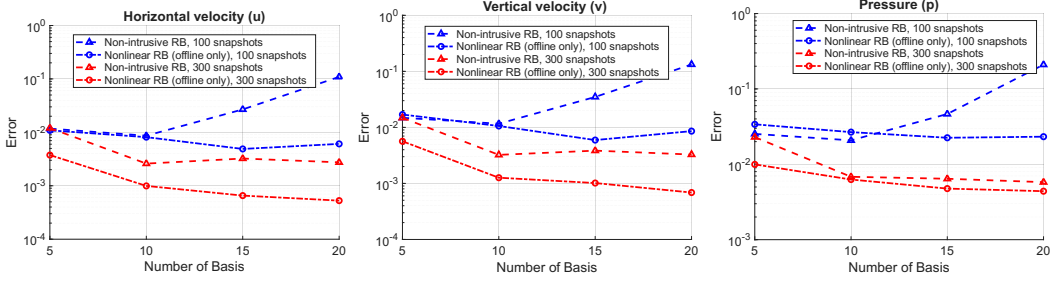


Figure 8: Relative errors of the offline-computed solutions as a function of the number of basis functions. From left to right, the plots show the results for horizontal velocity, vertical velocity, and pressure.

For computationally expensive parametrized PDEs such as the one in this example, it is often impractical to assume that a sufficient number of high-fidelity solutions (i.e., snapshots) can be generated. Therefore, it is informative to evaluate the performance of RB methods under varying number of available snapshots. In our experiments, we consider two snapshot sizes: 100 and 300.

We first consider the offline reconstruction NN model and compare its results with the non-intrusive RB method, using 100 randomly generated realizations of the PDE parameters. In Fig. 8, we plot the relative errors of both methods against the number of basis functions. This figure shows that for all solution components (i.e., for u , v and p), the approximations generated from 300 snapshots have smaller relative errors than the approximations obtained from 100 snapshots. This indicates that the performance of all tested reduced models is sensitive to the snapshot size. Moreover, we

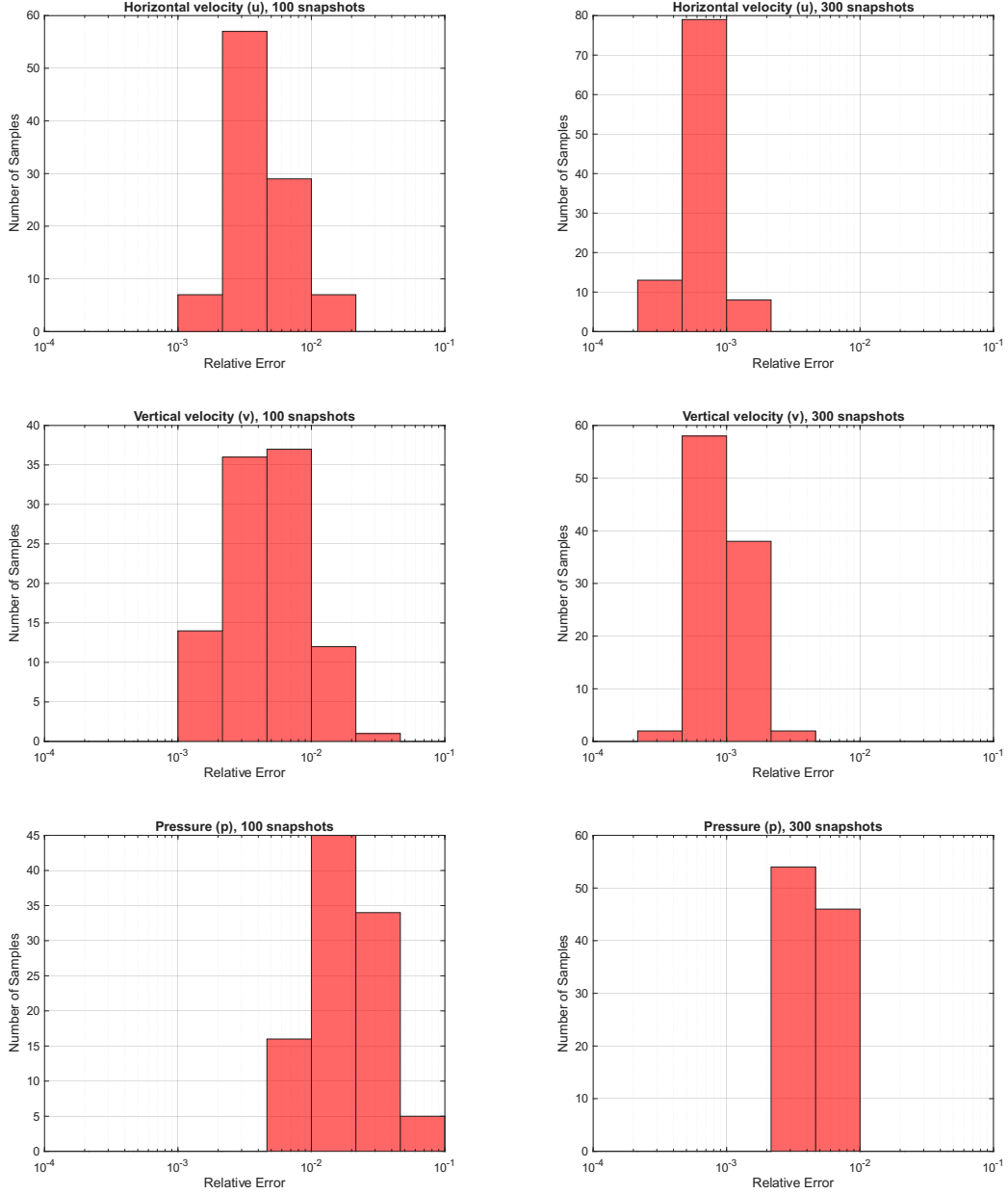


Figure 9: Histograms of the relative errors (over 100 samples) from the offline training results. The left column corresponds to predictions trained with 100 snapshots, and the right column to those with 300 snapshots. From top to bottom, the rows show the results for the horizontal velocity, vertical velocity, and pressure.

can see from Fig. 8 that the nonlinear RB method consistently achieves lower errors than the non-intrusive RB method for a fixed snapshot size, suggesting that it can capture the underlying solution structure more effectively in this example. Another aspect illustrated in Fig. 8 is how the size of the reduced basis affects the method’s performance: while increasing the size of the reduced basis generally reduces the error, especially for the nonlinear RB method, non-intrusive RB methods can exhibit strong non-monotonic behaviour, particularly when the number of snapshots is limited. These results show that the nonlinear RB method is more robust with respect to the snapshot size, largely due to its more flexible dependence on the snapshot data. Finally, the errors in all cases remain relatively large, which suggests that further online training is necessary to improve the accuracy of the reduced model. This point can be further illustrated by Fig. 9, which shows the histograms of the relative errors for u , v , and p , respectively. If we use 10^{-3} as a threshold, the relative errors for a large number of test samples exceed this value, especially in the case with 100 snapshots. These results further confirm that offline computation alone is often insufficient to ensure high accuracy, particularly when the number of snapshots is limited.

Next, we examine the results of the online adaptation using the same 50 test samples that were used to evaluate the offline results. First, as mentioned in Section 3, an important task of the offline model is that it can provide good initialization for the online adaptation. This is particularly important for complex problems, where online training can be highly expensive. We now demonstrate the effectiveness of this strategy through numerical test results. Namely, we conduct online adaptation on three examples that are randomly chosen from the test set and plot the validation loss as a function of the number of epochs in Fig. 10. The results show how fast the reconstruction models improve during the online training process. In particular, we conclude that the offline prediction provides a significantly lower loss compared to the tested random initialization. More importantly, it leads to much faster convergence: if we use 10^{-4} as the stopping threshold, the loss drops below 10^{-4} within 10^4 epochs in test examples 2 and 3, and within 4×10^4 epochs in example 1, whereas the random initialization converges more slowly and remains above the 10^{-4} threshold for all three examples. We also aim to provide a visual comparison of the online and offline results using these three examples. In Fig. 11, we present the velocity field and the pressure for these samples as computed by the offline model, the online model, and the high-fidelity solver. In Fig. 12, we show the spatial error maps in pressure for both

	$r = 5$	$r = 10$	$r = 15$	$r = 20$
300 snapshots	6	15	21	21
100 snapshots	4	7	7	7

Table 1: Offline training time (in hours).

the offline and online models, evaluated against the high-fidelity solutions. The plots demonstrate that in the three examples, online adaptation yields clear improvements.

We now evaluate the performance of the online adaption over all the 100 test samples. In Fig. 13, we plot the relative errors of the offline-only predictions and those with online adaptation, against the number of RB functions. The results are shown for the average error over all test samples and the average error over the 10 worst-case samples having the largest offline prediction errors. We present these results for both the 100-snapshot case (Fig. 13a) and the 300-snapshot case (Fig. 13b). As shown in the figure, in most cases the online adaptation further improves the accuracy of the reduced models. The improvement is particularly evident for the worst-case samples, where offline errors are the largest. Moreover, the effect of online adaptation is clearly more significant in the 100-snapshot case, indicating that online adaptation becomes particularly necessary when snapshot data are limited.

Finally, we discuss the computational cost of solving the parametrized PDE problem in this example. We report wall-clock times based on our specific computational setup, as detailed in Appendix A. Generating a single high-fidelity snapshot typically takes between 4 to 5 hours. The time required for offline training is reported in Table 1. The time for online adaptation varies across different test samples, and Fig. 14 shows the histograms of online training times for the 50 test examples, for both the 100-snapshot (left) and 300-snapshot (right) cases. The figure shows that, in both cases, the online training takes no more than 1600 seconds, which is considerably more efficient than using the conventional solver that typically requires several hours. Moreover, the online training time in the 100-snapshot case is generally longer than in the 300-snapshot case, indicating that when the number of snapshots is limited, online adaptation is particularly needed for achieving reliable results.

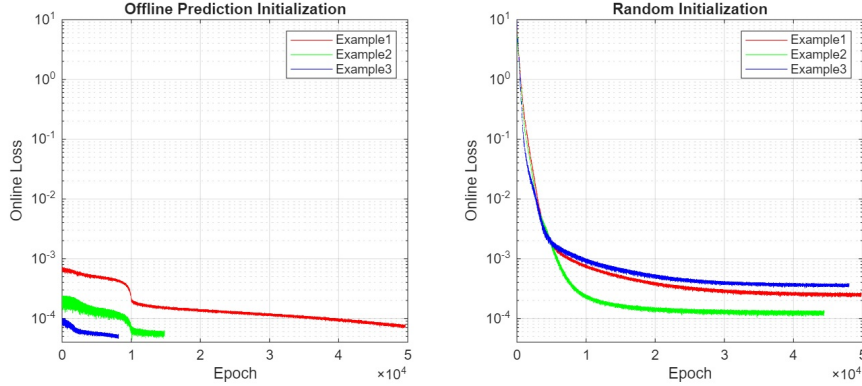


Figure 10: Online training loss plotted against the number of epochs for three test examples.

5 Conclusions

In this work, we have proposed a novel NN-based nonlinear RB method with online adaptation for efficient numerical solution of parametrized PDEs. The method integrates the strengths of non-intrusive RB approaches and PINNs, enabling both fast offline training and accurate online refinement. Unlike many existing methods that rely on linear combinations of basis functions, our approach employs a nonlinear mapping that better captures complex solution manifolds. The online adaptation stage leverages lightweight PINN-style training to refine predictions in an unsupervised manner, ensuring robustness and improving accuracy, even when offline-trained NN models are insufficient. Through numerical experiments on both a parametrized Burgers' equation and a multi-parameter lid-driven cavity problem, we have demonstrated that the proposed method achieves high accuracy with significantly reduced computational cost. In particular, the online stage has proved especially important in scenarios involving complex solution structures or limited snapshot data, where it has substantially enhanced the reliability and efficiency of predictions.

There are several possible directions for extending and improving the proposed method. First and foremost, while in this work we have restricted ourselves to steady-state PDE problems, a natural extension is to consider unsteady, or time-dependent, PDE systems, where the reduced model must evolve in time. This could be achieved by incorporating several tech-

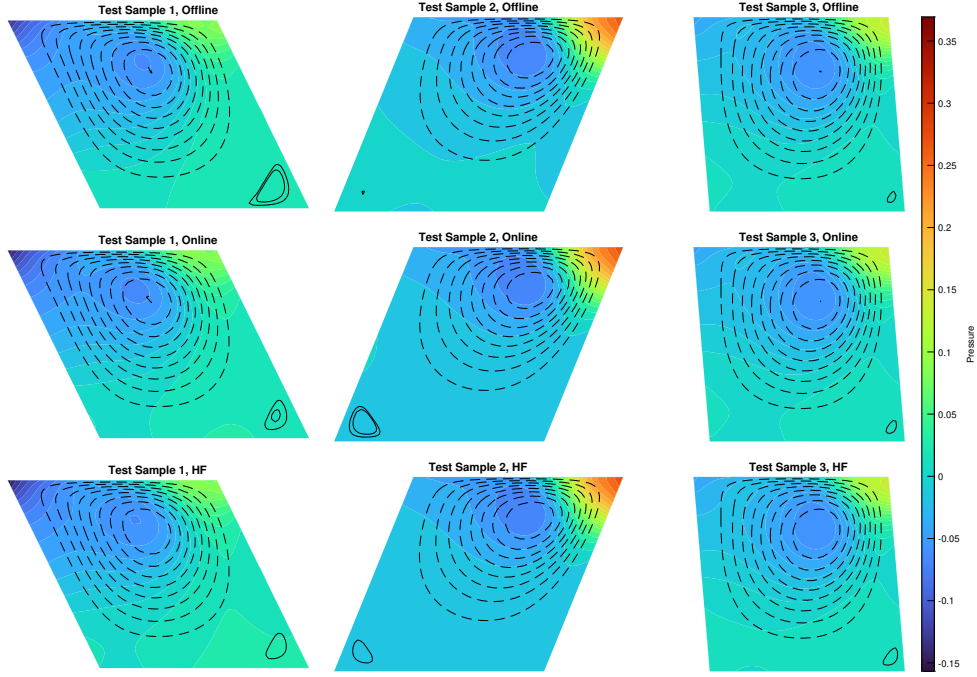


Figure 11: The velocity-pressure solutions to the lid-driven cavity problem. Each column corresponds to one of three test examples. From top to bottom, three rows show the results from the offline-computed model, the online-computed model, and the high-fidelity reference solution. The streamlines represent the velocity field (flow direction and structure), while the color map represents the pressure distribution.

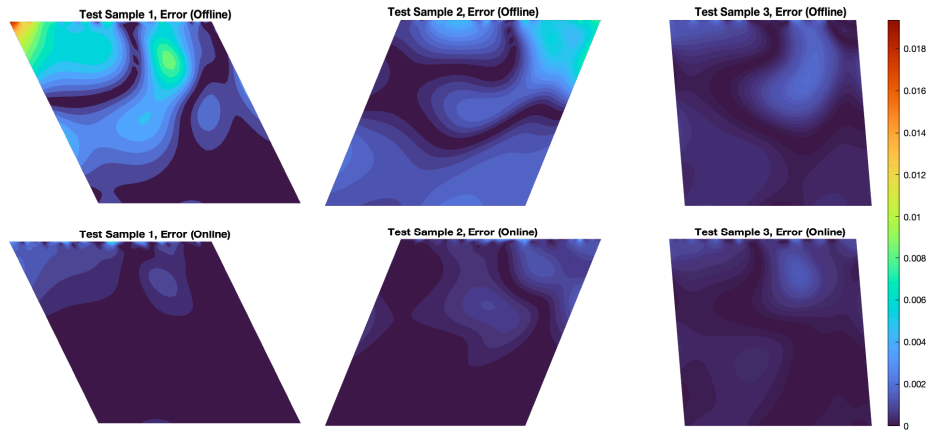
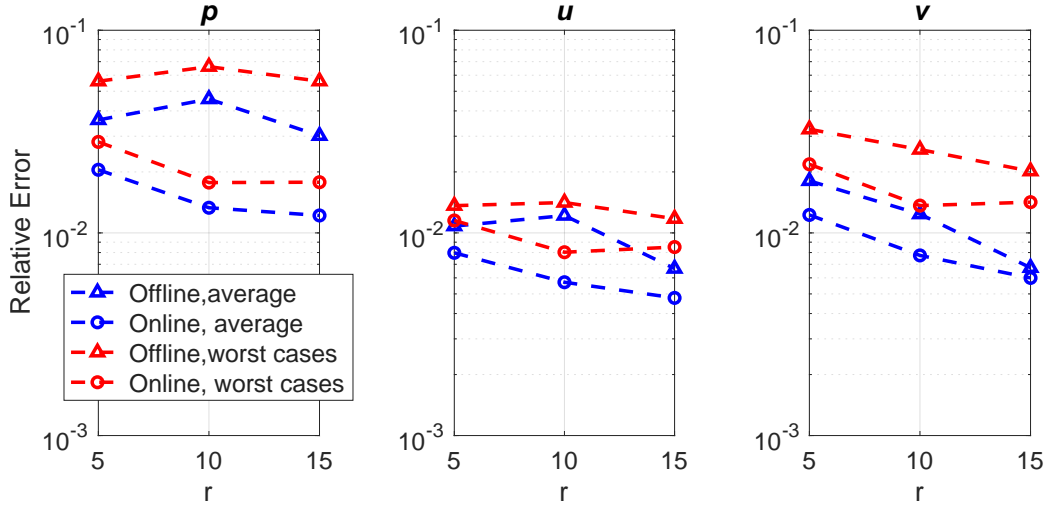
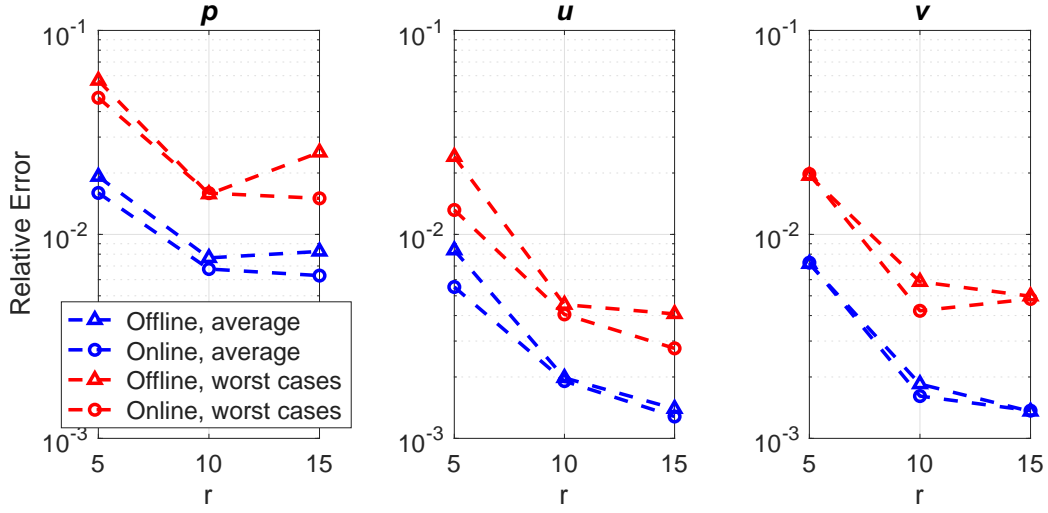


Figure 12: Relative error maps for the pressure in three test examples: the top row shows the results of the offline only predictions, while the bottom row shows the results where online adaptation is included.



(a) Results for the case with 100 snapshots



(b) Results for the case with 300 snapshots

Figure 13: Relative errors in the solution components reconstructed using the offline stage only versus those with online adaptation.

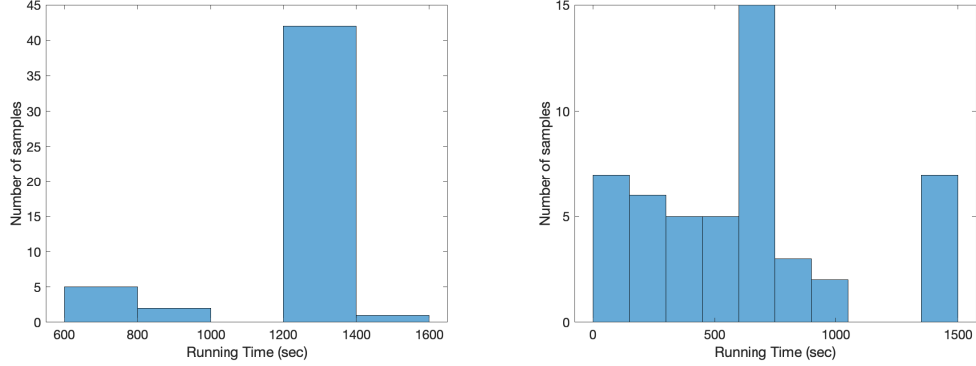


Figure 14: Histograms of online training times for 50 test examples. Left: the results for 100 snapshots and 10 basis functions. Right: the results for 300 snapshots and 15 basis functions.

niques that have been developed for time-dependent PDEs or dynamical systems [21, 30]. Second, the method can be linked to recent developments in operator-based neural networks, such as DeepONets [22, 23] and neural operators [20], which may offer improved generalization capabilities. Third, in the present formulation, the dimension reduction network is chosen to be independent of the model parameters, and so are the obtained basis functions. Alternatively, introducing parameter-dependent reduced bases or nonlinear dimension reduction could enable the model to better capture local features of the solution manifold and handle problems with strong transport or discontinuities [24, 31, 9]. Finally, the proposed approach is well suited for such real-world applications as Bayesian inference or inverse problems, where its non-intrusive and adaptive nature may significantly accelerate posterior sampling or optimization. These directions will further broaden the applicability and impact of the proposed method across scientific and engineering domains, and we will explore them in future work.

A Implementation details

In this section, we briefly provide the implementation details of our numerical experiments. All experiments were conducted on a computing node equipped with dual-socket Intel(R) Xeon(R) Platinum 8360Y CPUs (2.40 GHz, 72 cores in total), with 28 cores allocated for the computations. The system also includes an NVIDIA A100-SXM4-40GB GPU and 503 GiB of RAM.

Code and data : <https://github.com/hzjy2025/nonintrusive25>. This code is based on and extends the given code by [8].

In both numerical examples, we use same the network architectures, which are detailed below.

The *dimension reduction* model Φ in (3.1) consists of one fully connected layer with Swish activation [25], followed by an output layer with no activation. This network has ℓ input neurons, r neurons at the hidden layer and r outputs. We fix $\ell = 20$ in our experiments and study the performance of the model for different values of r .

The *solution reconstruction* model U (see (3.2)) is a one hidden layer network with r inputs, 5 hidden neurons and one output. The activation used is Tanh [25]. We emphasize that this network is deliberately kept simple as it needs to be trained online.

The input dimension of the *parameter estimation* model Θ (see (3.3)) is equal to the dimension of the parameter domain; this model has four hidden layers with 100 neurons each. The activation after each hidden layer is Swish. The number of outputs of Θ is the total number of network parameters in U . Specifically, U is represented by two weight matrices and two bias vectors, so the total number of network parameters is $5r + 11$. In the lid-driven cavity example where we want to predict the pressure and two components of the velocity field, we use three models with the same structure as the one discussed above. Each model corresponds to one output.

In both test examples, the networks are trained in the offline stage using the loss function (3.5) with $p = 1$. In the first example, we set $\lambda_0 = 1$ and $\lambda_1 = 0.001$ in (3.5). In the second example where the PDE model is two-dimensional, we set $\lambda_{(0,0)} = 1$ and $\lambda_{(1,0)} = \lambda_{(0,1)} = 0.001$.

In the second example, the pressure is determined up to an additive constant; see, e.g. [18]. To account for this, we compute the integral of the pressure function over the domain using the Clenshaw–Curtis quadrature and shift the function so that it has zero mean. We do this for all computed pressure functions, whether obtained using the proposed method or a stand-

ard PDE solver, and then measure the error between the shifted functions.

References

- [1] O. BOTELLA AND R. PEYRET, *Benchmark spectral results on the lid-driven cavity flow*, Computers & Fluids, 27 (1998), pp. 421–433.
- [2] C.-H. BRUNEAU AND M. SAAD, *The 2d lid-driven cavity problem revisited*, Computers & fluids, 35 (2006), pp. 326–348.
- [3] S. CAI, Z. MAO, Z. WANG, M. YIN, AND G. E. KARNIADAKIS, *Physics-informed neural networks (PINNs) for fluid mechanics: a review*, Acta Mech. Sin., 37 (2021), pp. 1727–1738.
- [4] K. CARLBERG, C. BOU-MOSLEH, AND C. FARHAT, *Efficient non-linear model reduction via a least-squares Petrov-Galerkin projection and compressive tensor approximations*, Internat. J. Numer. Methods Engrg., 86 (2011), pp. 155–181.
- [5] F. CASENAVE, A. ERN, AND T. LELIÈVRE, *A nonintrusive reduced basis method applied to aeroacoustic simulations*, Adv. Comput. Math., 41 (2015), pp. 961–986.
- [6] S. CHATURANTABUT AND D. C. SORESENSEN, *Nonlinear model reduction via discrete empirical interpolation*, SIAM J. Sci. Comput., 32 (2010), pp. 2737–2764.
- [7] W. CHEN, J. S. HESTHAVEN, B. JUNQIANG, Y. QIU, Z. YANG, AND Y. TIHAO, *Greedy nonintrusive reduced order model for fluid dynamics*, AIAA Journal, 56 (2018), pp. 4927–4943.
- [8] W. CHEN, Q. WANG, J. S. HESTHAVEN, AND C. ZHANG, *Physics-informed machine learning for reduced-order modeling of nonlinear problems*, J. Comput. Phys., 446 (2021), pp. Paper No. 110666, 28.
- [9] Y. CHEN, Y. JI, A. NARAYAN, AND Z. XU, *TGPT-PINN: nonlinear model reduction with transformed GPT-PINNs*, Comput. Methods Appl. Mech. Engrg., 430 (2024), pp. Paper No. 117198, 20.

- [10] Y. CHEN AND S. KOOHY, *GPT-PINN: generative pre-trained physics-informed neural networks toward non-intrusive meta-learning of parametric PDEs*, Finite Elem. Anal. Des., 228 (2024), pp. Paper No. 104047, 15.
- [11] J. W. DEMMEL, *Applied numerical linear algebra*, SIAM, 1997.
- [12] S. FRESCA, L. DEDÉ, AND A. MANZONI, *A comprehensive deep learning-based approach to reduced order modeling of nonlinear time-dependent parametrized PDEs*, J. Sci. Comput., 87 (2021), pp. Paper No. 61, 36.
- [13] S. FRESCA AND A. MANZONI, *POD-DL-ROM: enhancing deep learning-based reduced order models for nonlinear parametrized PDEs by proper orthogonal decomposition*, Comput. Methods Appl. Mech. Engrg., 388 (2022), pp. Paper No. 114181, 27.
- [14] I. GOODFELLOW, Y. BENGIO, AND A. COURVILLE, *Deep learning*, MIT press, 2016.
- [15] M. GUO AND J. S. HESTHAVEN, *Reduced order modeling for nonlinear structural analysis using Gaussian process regression*, Comput. Methods Appl. Mech. Engrg., 341 (2018), pp. 807–826.
- [16] ———, *Data-driven reduced order modeling for time-dependent problems*, Comput. Methods Appl. Mech. Engrg., 345 (2019), pp. 75–99.
- [17] J. S. HESTHAVEN, G. ROZZA, AND B. STAMM, *Certified reduced basis methods for parametrized partial differential equations*, vol. 590, Springer, 2016.
- [18] J. S. HESTHAVEN AND S. UBBIALI, *Non-intrusive reduced order modeling of nonlinear problems using neural networks*, J. Comput. Phys., 363 (2018), pp. 55–78.
- [19] T. J. HUGHES, *The finite element method: linear static and dynamic finite element analysis*, Courier Corporation, 2003.
- [20] N. KOVACHKI, Z. LI, B. LIU, K. AZIZZADENESHELI, K. BHATTACHARYA, A. STUART, AND A. ANANDKUMAR, *Neural operator: learning maps between function spaces with applications to PDEs*, J. Mach. Learn. Res., 24 (2023), pp. Paper No. [89], 97.

- [21] K. LEE AND K. T. CARLBERG, *Model reduction of dynamical systems on nonlinear manifolds using deep convolutional autoencoders*, J. Comput. Phys., 404 (2020), pp. 108973, 32.
- [22] L. LU, P. JIN, AND G. E. KARNIADAKIS, *DeepONet: Learning nonlinear operators for identifying differential equations based on the universal approximation theorem of operators*, arXiv preprint arXiv:1910.03193, (2019).
- [23] L. LU, P. JIN, G. PANG, Z. ZHANG, AND G. E. KARNIADAKIS, *Learning nonlinear operators via DeepONet based on the universal approximation theorem of operators*, Nature machine intelligence, 3 (2021), pp. 218–229.
- [24] N. J. NAIR AND M. BALAJEWICZ, *Transported snapshot model order reduction approach for parametric, steady-state fluid flows containing parameter-dependent shocks*, Internat. J. Numer. Methods Engrg., 117 (2019), pp. 1234–1262.
- [25] C. NWANKPA, *Activation functions: Comparison of trends in practice and research for deep learning*, arXiv preprint arXiv:1811.03378, (2018).
- [26] G. PADULA, M. GIRFOGLIO, AND G. ROZZA, *A brief review of reduced order models using intrusive and non-intrusive techniques*, PAMM, 24 (2024), p. e202400210.
- [27] F. PICHI, B. MOYA, AND J. S. HESTHAVEN, *A graph convolutional autoencoder approach to model order reduction for parametrized PDEs*, J. Comput. Phys., 501 (2024), pp. Paper No. 112762, 24.
- [28] A. QUARTERONI, A. MANZONI, AND F. NEGRI, *Reduced basis methods for partial differential equations: an introduction*, vol. 92, Springer, 2015.
- [29] M. RAISSI, P. PERDIKARIS, AND G. E. KARNIADAKIS, *Physics-informed neural networks: a deep learning framework for solving forward and inverse problems involving nonlinear partial differential equations*, J. Comput. Phys., 378 (2019), pp. 686–707.
- [30] F. REGAZZONI, L. DEDÈ, AND A. QUARTERONI, *Machine learning for fast and reliable solution of time-dependent differential equations*, J. Comput. Phys., 397 (2019), pp. 108852, 26.

- [31] D. RIM, B. PEHERSTORFER, AND K. T. MANDLI, *Manifold approximations via transported subspaces: model reduction for transport-dominated problems*, SIAM J. Sci. Comput., 45 (2023), pp. A170–A199.
- [32] Q. WANG, J. S. HESTHAVEN, AND D. RAY, *Non-intrusive reduced order modeling of unsteady flows using artificial neural networks with application to a combustion problem*, J. Comput. Phys., 384 (2019), pp. 289–307.
- [33] D. XIAO, P. YANG, F. FANG, J. XIANG, C. C. PAIN, AND I. M. NAVON, *Non-intrusive reduced order modelling of fluid-structure interactions*, Comput. Methods Appl. Mech. Engrg., 303 (2016), pp. 35–54.
- [34] J. YU, C. YAN, AND M. GUO, *Non-intrusive reduced-order modeling for fluid problems: A brief review*, Proceedings of the Institution of Mechanical Engineers, Part G: Journal of Aerospace Engineering, 233 (2019), pp. 5896–5912.